

Patch-Probe Excitation for Ultrahigh Magnetic Field Wide-Bore MRI

Patrick Bluem, *Graduate Student Member, IEEE*, Andrew Kiruluta, Pierre-Francois Van de Moortele, Allison Duh, *Member, IEEE*, Gregor Adriany, *Member, IEEE*, and Zoya Popović, *Fellow, IEEE*

Abstract—In this paper, we present the design of probe excitations for 7- and 10.5-T traveling-wave wide-bore magnetic resonance imaging systems. The probes are 297- and 447-MHz coaxially fed microstrip patches, designed to give a circularly polarized magnetic field when placed in the metallic bore waveguide. Images of a water phantom using the patch probes are obtained and compared with full-wave electromagnetic simulations. Additionally, periodic axial metal strip cylinders are inserted into the bore, resulting in improved field uniformity in a phantom with a simultaneous increase in SNR. The numerical analysis for nonquasi-static fields can be computationally intensive, and the numerical error for finite-element simulations is quantified using modified boundary conditions of the system. When the waveguide effects are taken into account, the mode content in the images compares well to full-wave simulations.

Index Terms—FEM, magnetic resonance imaging (MRI), patch antenna, waveguide.

I. INTRODUCTION

CURRENT clinical magnetic resonance imaging (MRI) scanners operate at low frequencies, 64 MHz for 1.5 T and 128 MHz for 3 T, where the imaging volume is electrically small. This allows the use of a quasi-static approximation for design of reactive near-field RF excitation coils [1]–[4]. For these systems, uniform spatial coverage is achieved by phasing reactive near-field coils; however, this approach is only valid when the imaging volume is electrically small. For higher static magnetic fields of 7 and 10.5 T, desired for higher resolution, the imaging volume of a wide-bore system is larger than a wavelength and the bore becomes an overmodeled waveguide that can benefit from a traveling-wave excitation, as demonstrated in [5] and [6]. The use of traveling-wave excitations can increase the spatial coverage of a single probe in samples that are larger than the wavelength of the NMR signal. In this paper, experiments use a whole-body

Manuscript received August 10, 2016; revised October 18, 2016 and December 10, 2016; accepted December 10, 2016. Date of publication February 14, 2017; date of current version June 29, 2017. This work was supported in part by the National Science Foundation under Collaborative Research Grant ECCS 1307614 at the University of Colorado, Boulder, and in part by the National Institutes of Health under Grant P41 EB015894 and Grant S10 RR029672.

P. Bluem, A. Duh, and Z. Popović are with the Department of Electrical, Computer, and Energy Engineering, University of Colorado Boulder, Boulder, CO 80309-0425 USA (e-mail: zoya.popovic@colorado.edu).

A. Kiruluta is with the Department of Physics, Harvard University, Cambridge, MA 02138 USA.

P.-F. Van de Moortele and G. Adriany are with the Center for Magnetic Resonance Research, Department of Radiology, University of Minnesota, Minneapolis, MN 55455 USA.

Color versions of one or more of the figures in this paper are available online at <http://ieeexplore.ieee.org>.

Digital Object Identifier 10.1109/TMTT.2017.2656084

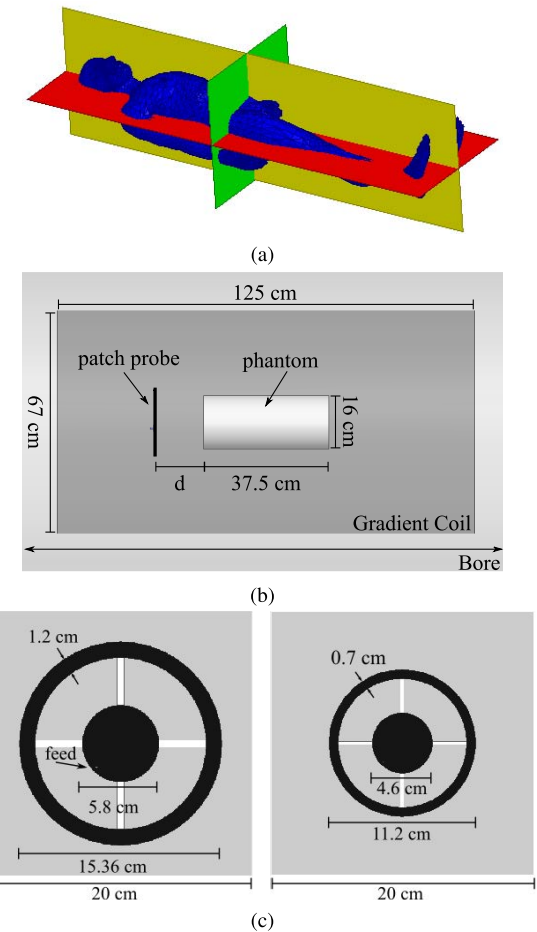


Fig. 1. (a) Plane definitions for sagittal (yellow), coronal (red), and axial (green) cross sections. (b) Sagittal view of the dimensions under the gradient coil for both 7- and 10.5-T Siemens systems. The dark gray region is the region internal to the gradient coil. (c) 7 T (left, 297 MHz) and 10.5 T (right, 447 MHz) circular patch probes. Black indicates top metal, gray is the ground plane, and the white rectangles are slots in the ground plane, and the dimensions are given for an FR-4 substrate.

Siemens 7-T system equipped with an Agilent magnet with a bore that is 3.366 m in length with a diameter of 90 cm. The Larmor frequency at 7 T is 297 MHz, corresponding to a free-space wavelength of 1.01 m and a wavelength in the water-based phantom ($\epsilon_r = 81$) of 11.22 cm. The 90-cm open bore fits a human and is above the cutoff frequency for at least one mode of the bore when viewed as a cylindrical metallic waveguide loaded with a high dielectric constant, such as biological tissue, Fig. 1.

The motivations for using high dc magnetic flux density ($B_0 > 3$ T) include increased SNR [7], allowing for improved

spatial resolution [8], [9], better parallel imaging performance and potential for improved contrast [10]. Traveling-wave MRI has been successfully demonstrated at various field strengths, including wide-bore 7 and 9.4 T [5], [11], [12] and small-bore animal 16- and 21.1-T systems [13]. Current clinical machines and small-bore systems do not support traveling waves unless high dielectric inserts [14] or coaxial transmission lines [15] are added for mode propagation. The addition of dielectric loading [16]–[18] or multiple excitations [19] can be used in ultrahigh field systems to help improve homogeneity; however, these solutions can be large and heavy.

Several RF probe designs have been used in high-magnetic field MR systems, including loop coils [20], electric dipoles [21], standard patch antennas [5], [19], [22], microstrip radiators [23]–[25], coaxial waveguide [18], and monofilar helix [26]. These probes couple energy to the loaded waveguide modes, with the goal of providing as uniform of a circularly polarized B -field as possible inside the object to be imaged. A circular polarization in the direction of the precession of the spins is required to excite the protons in the imaging volume. A few different methodologies have been used for microstrip radiator arrays. Simple straight parallel microstrip lines are not effective, since the B -field generated is not balanced across the whole line. One method to improve the uniformity across the line uses a trapezoidal shape [23] to tailor the field to be uniform across the line. A high degree of isolation is also desired between elements, which is typically achieved with decoupling networks using lumped capacitors and inductors [27]; however, this technique can lead to a large separation between elements or small component values at high fields that may not be realizable. Another method to improve coupling to the imaging volume is adding more elements; however, the close proximity of elements reduces isolation. Reference [24] alternates between the first and second harmonic microstrip elements to increase the number of elements to 16, with a simultaneous increase in the number of elements and the isolation.

In [28], the design of a patch-based probe for a 16.4-T small-bore animal MRI system is demonstrated and showed high SNR improvements compared with loop-based probes thus enabling the first reported true spin echo (180° pulse refocusing) measurement with a traveling-wave setup. Spin echo measurements often cannot be obtained with traveling-wave excitation because of insufficient RF transmission into the sample, requiring excessive RF power. Here, we present extensions of this paper to human-size (67-cm diameter) bore 7- and 10.5-T systems.

This paper is organized as follows. In Section II, the overall system geometry and probe layout are given, along with additional modifications of the bore, such as copper strip arrays and electrically hard surfaces, which enable improved field uniformity. Section III details simulations and measurements on the 7-T system, including dependence of image quality on geometric parameters, such as probe distance from phantom and boundary condition modification. Section IV presents multiple probe transmit and receive results at 7 T, including experimental and simulated observations related to relative phasing between the two. Section V summarizes results for the

10.5-T system, and, finally, Section VI presents a discussion on the numerical analysis. For all simulations presented here, Ansys high frequency structural simulator (HFSS) full-wave electromagnetic finite-element solver is used. Gradient nonlinearities are not corrected for, resulting in well-known barrel-shaped experimental image distortion instead of a correct restitution of the cylindrical shape of the physical phantom.

II. SYSTEM AND PROBE LAYOUT

The systems used in this paper are two whole body human dimensioned (67-cm bore) MR scanners operating at 7 and 10.5 T (Siemens, Erlangen, Germany). The spin excitation (Larmor) frequency is determined by

$$f = \gamma B_0 \quad (1)$$

where γ is the gyromagnetic ratio and B_0 is the static magnetic field. Using the gyromagnetic ratio of hydrogen, $\gamma = 42.58 \text{ MHz/T}$, the proton Larmor frequency is calculated to be 297 MHz at 7 T and 447 MHz at 10.5 T [1]. Whole body MR systems, including high field, are built around wide-bore magnets that accommodates the size of a human body. In MRI, slice orientations include three orthogonal planes defined as sagittal, coronal, and axial as shown in Fig. 1(a), dividing the body in left and right, anterior and posterior, cranial and caudal portions, respectively. Sagittal cuts crossing the magnet isocenter will be presented in the remainder of this paper, as single coronal cuts centered cuts missed the phantom isocenter due to an off-centered elevation of the phantom holder in the vertical direction.

Circular patch antennas have been used in traveling-wave MRI [5] due to the circular nature of the currents and higher directivity than dipoles of the same size fed in quadrature. Although some antenna theory and approaches are used in the design of the patch, it is not actually an antenna in free space, but rather a probe that couples to modes in the loaded bore waveguide. Therefore, the modeling is done with a metal cylinder the size of the bore, and the distance to the phantom is varied to verify the traveling-wave conditions. Coupling of the circularly polarized magnetic field into the phantom is examined in simulations by observing the transverse components of the B -field.

A. System Dimensions

The wide-bore system in Fig. 1(b) shows the relevant dimensions and position in the bore of the gradient coil, the water phantom, and patch probe. The two systems are nearly identical dimensionally (both are equipped with the same gradient coil), other than the complete bore length. The 7-T system is 336.5 cm long while the 10.5-T system is longer by about one-fifth, at 410 cm. The electrical lengths are, however, greatly different, thus producing different mode structures. The cutoff frequency for the TE_{11} mode of the air-filled circular waveguide (bore) can be calculated using [29]

$$f = \frac{0.293}{a\sqrt{\mu\epsilon}} \quad (2)$$

where a is the radius of the waveguide. For the 7-T system, the cutoff frequencies are found to be 199.8 MHz in

the bore and 262.4 MHz inside the gradient coil. With the addition of a high permittivity dielectric, the cutoff frequencies will decrease, allowing for the propagation of additional modes. The first four propagating modes for a 7-T MRI are solved for in [30] to be HE₁₁, TE₀₁, HE₂₁, and TM₀₁. The high attenuation of the first four modes shows that the excitation source must be close to the phantom, but not so close that traveling-wave conditions are not met. Necessary computational resources in simulations are substantially minimized by excluding physical components, such as the plastic bore cover and patient table, that are structurally complicated to mesh but electrically insignificant as shown later in Section III. The phantom used for experiments is the Siemens 55 12 608 K2205, which is 16 cm in diameter and 37.5 cm long. This phantom is approximated by a cylinder of the same dimensions with a dielectric permittivity of $\epsilon_r = 81$ and a conductivity of $\sigma_d = 0.4$ S/m.

B. Circular Patch Probe

A circular patch with an outer ring and slots is chosen as an excitation source due to the circular nature of the current on the patch and compact design [31]. The uneven slots in the ground plane enable single coaxial feed right-handed circular polarization. The probe is implemented using FR-4 62.5-mil-thick substrate with $\epsilon_r = 4.35$ at 297 MHz. The probe is designed using full-wave simulations for 297-MHz excitation with dimensions seen in Fig. 1(c). The 5.45-mm-wide slots in the ground plane are 15.4 and 15.22 cm long, creating a right-handed circular polarized current distribution, with the feed diagonally 2.55 cm from the center. The probe is fed using a coaxial feed using an SMA coaxial connector excites the inner circularly shaped metal. The single feed and uneven slots create a quadrature current excitation which enables circular polarization. For the opposite sense circular polarization, the feed can be moved 90° around the patch in either direction. The probe for 10.5 T is implemented using the same FR-4 substrate with a permittivity of $\epsilon_r = 4.25$. The dimensions can be seen in Fig. 1(c) with 2.5-mm-wide slots that are 11.25 and 11.03 cm long and the feed 2.05 cm from the center. The ground plane is much larger than necessary to provide mounting similar to the 7-T probe experiments. Both probes exhibited a measured narrowband 10-MHz bandwidth return loss greater than 15 dB with no additional matching inside the bore. The probe is placed at a distance d from the phantom as shown in Fig. 1(b). This distance varies depending on the experiment.

The quality of the near-field circular polarization is determined by the currents of the probe. Right-handed circular polarization is defined by the electric field tracing a clockwise circle from the receiver's point of view. The magnitude of the current density on the top conductors as the phase advances is shown in Fig. 2. The magnitude of the current density on the ground plane can be seen in Fig. 3. The slots behave similar to dipoles in quadrature where in Fig. 3(b) the current density fully illuminates the vertical slot. As the current advances 90°, the current density in Fig. 3(e) fully illuminates the horizontal slot. As a result of this behavior, the magnitude of the current

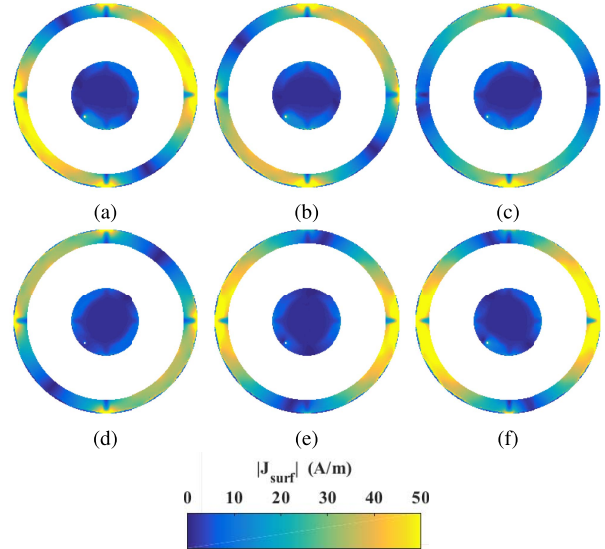


Fig. 2. Magnitude of the current density on the top conductors of the patch probe as the phase advances from (a) 0° to (f) 150° with a step size of 30° [indicated in black in Fig. 1(c)].

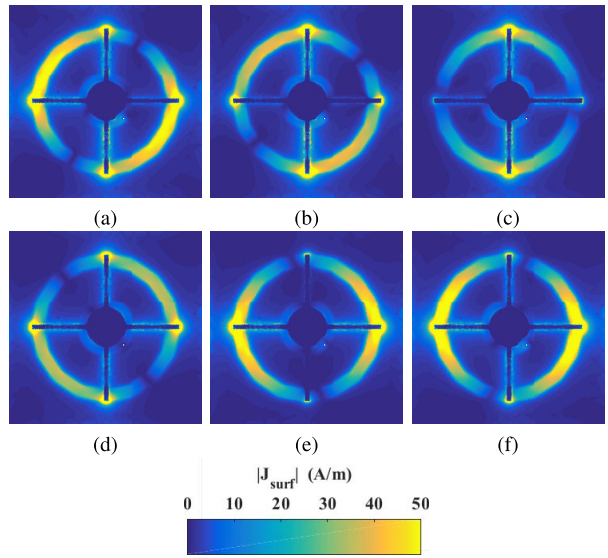


Fig. 3. Magnitude of the current density on the ground plane of the patch probe as the phase advances from (a) 0° to (f) 150° with a step size of 30° [shown in gray in Fig. 1(c)].

density traces an elliptical pattern. When simulated as an antenna, the probes exhibit a 1-dB far-field axial ratio.

C. Electrically Hard Surface

Experiments from [28] show that field coupling and distribution can be improved by modifying the modes in the bore through changing the boundary conditions. For example, electrically hard surfaces are used in horn antennas to increase aperture efficiency [32]. A longitudinally corrugated surface where the tangential electric and longitudinal magnetic fields are equal to zero along the surface is referred to as an electrically hard surface [33]. Electrically hard surfaces can either be formed by implementing dielectric-filled longitudinal

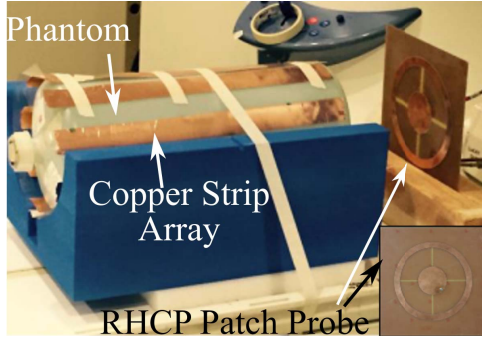


Fig. 4. Experimental setup of electrically hard surface approximated by thin copper strips on a plastic sheet on a 16-cm diameter phantom for a 7-T system. The probe used is shown in the bottom right.

corrugations or longitudinal conducting strips on a dielectric horn antenna [32].

For experiments presented in this paper, longitudinal conducting strips are implemented without a dielectric. Since it is an approximation to a hard surface, we refer to it as a copper strip array, and simulations show that only the magnitude of the fields is slightly affected by eliminating the dielectric. The longitudinal strips are implemented using copper tape on a thin plastic sheet and wrapped around the dielectric phantom, Fig. 4. The strips are 3 cm wide with 3 cm separation and the length is varied for different experiments.

III. 7-T SIMULATED AND EXPERIMENTAL RESULTS

The distance between the probe and the phantom is varied to help determine the optimal location for the best signal strength and SNR. The copper strip structure is then set up in various configurations to analyze the effect on SNR and signal intensity. All images are taken using a gradient recalled echo sequence for an FOV of $20 \times 40 \text{ cm}^2$ with a small flip angle. This small flip angle regime preserves direct proportionality between the magnitude of the detected MR signal originating inside the phantom and the corresponding excitation field magnitude distribution. Note that the detected signal is also proportional to the receive field magnitude and to the proton density of the phantom.

The probe is placed $d = 15 \text{ cm}$ from the phantom and simulated to measure the effects of several extra physical features as shown in Fig. 5. The features modeled include the plastic covering over the gradient coil, the foam that is used to support the cylindrical phantom, and the plastic patient table. Fig. 6 shows the result with and without the extra features modeled. The extra features cause an asymmetry in the fields toward the foam holder (left side of the plot), deforming the center mode pattern from the oval shape shown in Fig. 6(b). The result shown in Fig. 6(b) is used as the basis for comparing all results.

A. Distance Sweep From the Phantom

With its long axis parallel to the long axis of the magnet, the phantom is positioned at the center of the latter along the foot-head direction, and slightly off-centered above the

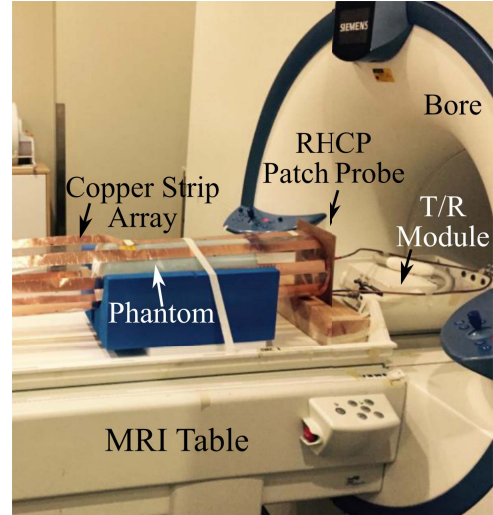


Fig. 5. Complete setup showing the probe and phantom on the Siemens table and connected to the T/R switch. The copper strip array covers both the air gap and phantom.

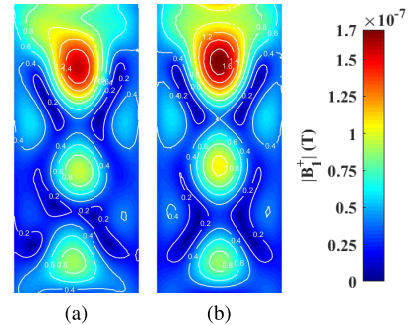


Fig. 6. 7-T simulations of the probe 15 cm from the phantom (a) with and (b) without modeling the plastic covering over the gradient coil, foam phantom support, and table. Normalized to 1-W input power at the probe port.

patient table, held within a foam holder. The phantom is imaged at several distances from the patch probe: the location closest to the phantom ($d = 4.5 \text{ cm}$); the farthest possible location ($d = 40 \text{ cm}$); and two distances in between ($d = 15$ and 25 cm).

The experimental results, Fig. 7, are plotted as magnitude images using a DICOM viewer and individually scaled to show the overall mode pattern. The first distance, $d = 4.5 \text{ cm}$ and Fig. 7(a), shows a vertical asymmetry in the mode pattern, corresponding to a degradation in the circular polarization, which results in wasted power in the cross-polarized field. The second distance, $d = 15 \text{ cm}$ and Fig. 7(b), shows excellent matching with the simulated mode pattern [Fig. 6(b)], with reasonable SNR. The image, however, is slightly skewed due to the physical mounting of the probe. The semirigid cables and magnetic solder prevent perfect vertical positioning of the probe and the foam phantom holder creates a material discontinuity. The next distance, $d = 25 \text{ cm}$ and Fig. 7(c), shows a similar image to the 15 cm case but of slightly lower magnitude and SNR. The last case, $d = 40 \text{ cm}$ and Fig. 7(d), shows very little signal coupled and low SNR. These results

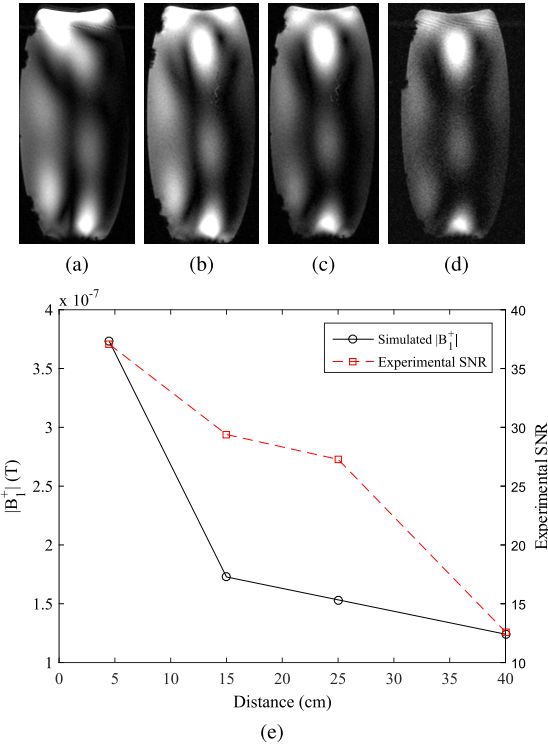


Fig. 7. MR images plotted to show the mode pattern variation for different d values [Fig. 1(b)]. (a) 4.5 cm. (b) 15 cm. (c) 25 cm. (d) 40 cm. Images are individually scaled to show consistency in excited mode pattern with magnitude variations shown in (e). (e) Magnitude of the simulated response and SNR for the locations (a)–(d).

indicate that between 15 and 40 cm there is a consistent field profile based off the probe excitation and a traveling wave is indeed excited.

The magnitude of the simulated response is shown in Fig. 7(e) (left) and the SNR, Fig. 7(e) (right) calculated according to [34] with a 1-cm square box in the center mode pattern used for comparison. Distances between 15 and 25 cm are usable, with only limited magnitude variation and a preserved overall mode pattern. Beyond 25 cm, however, the distance is too long, leading to decreased signal strength, thus lower SNR, which translates into lower image quality. From these results, 15 cm is taken to be the best location and is used for future experiments.

The distance, d , between the phantom and the excitation plays two critical roles. First, the cross polarization effects and reflected power become greater as the probe moves closer to the phantom due to the large discontinuity of the high dielectric constant phantom. The farther the probe is from the phantom, the more consistent the frequency response and circular polarization will be for different dielectrics. Second, as the probe moves farther away, the SNR degrades due to the decrease in overall coupled field, but the peak magnitude (located close to the probe) stays fairly high. This field imbalance causes a degradation of the mode features farther into the phantom and produces an overall noisier image. The resulting pattern may be expected to be clinically unusable. Furthermore, there is a large deviation between the maxima and the middle and edge field magnitudes along with large

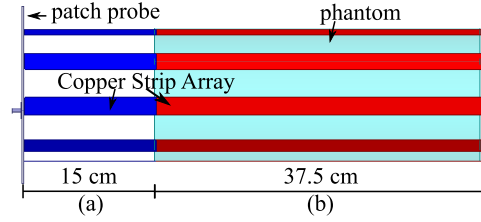


Fig. 8. Details the setup of copper strip experiments. (a) Air gap between the probe and phantom. (b) Phantom.

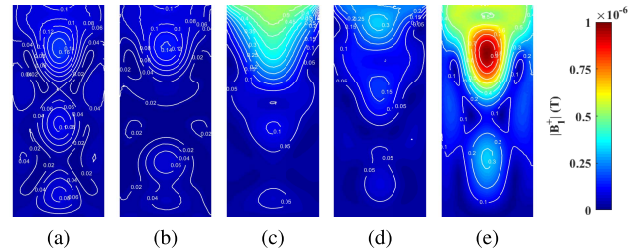


Fig. 9. Simulations of copper strip array experiments for (a) no copper structure, (b) 37.5-cm phantom, (c) 15-cm air gap, (d) 30-cm air gap, and (e) phantom and 15-cm air gap. Simulations are plotted on the same scale. Normalized to 1-W input power at the probe port.

gaps in field coverage. To remedy this deviation, the field should be homogenized, which can be addressed by changing the boundary conditions, as described next.

B. Copper Strip Array Experiments

Next, experiments are run with $d = 15$ cm and with the copper strip array (Fig. 4) for the following cases:

- (a) no copper strip array;
- (b) strips covering the 37.5-cm phantom [Fig. 8(b)];
- (c) strips covering the 15-cm air gap [Fig. 8(a)];
- (d) strips covering the 30-cm air gap;
- (e) strips covering the 15-cm air gap and phantom (Fig. 4).

The simulated results corresponding to the above-mentioned configurations are shown in Fig. 9. The magnitude of the field of the first strips experiment is similar to the case with no copper strip array, but broadens slightly at the top of the phantom and reduces the field away from the probe. The second strips experiment creates a classical near-field absorption parameter with high field concentrated close to the probe and little elsewhere as shown in Fig. 9(c). To try and balance the possible near-field pattern with the field in the rest of the phantom, the probe is moved out to $d = 30$ cm. Fig. 9(d) shows a result similar to Fig. 9(a) but with increased field strength, and a mode pattern which is more visible across the entire image compared with Fig. 9(c). The last case moves the probe back to $d = 15$ cm and uses the copper strip array covering the 15-cm air gap and the 37.5-cm phantom.

Experimentally, the copper strip array performs as expected, as shown in Fig. 10. For the first experiment, Fig. 10(b), the field coupling is comparable to Fig. 10(a), but the mode pattern has changed. The top mode pattern has spread, as expected with the copper strip array. The lower mode pattern is faint compared with the upper pattern, while the middle mode

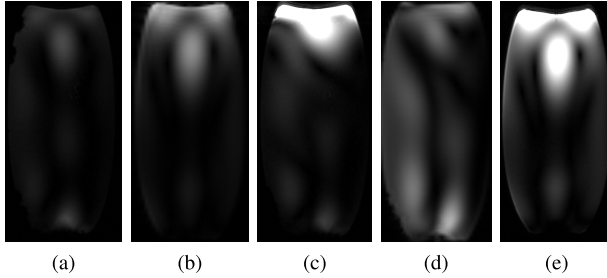


Fig. 10. MR images for (a) no copper structure, (b) 37.5-cm phantom, (c) 15-cm air gap, (d) 30-cm air gap, and (e) phantom and 15-cm air gap. MR images are plotted on the same scale.

TABLE I
SNR FOR SINGLE PROBE EXPERIMENTS

| Experiment | SNR |
|---------------------------------|-----|
| $d=15\text{cm}$ Fig. 10a | 46 |
| Copper Strip Array (b) Fig. 10b | 92 |
| Copper Strip Array (c) Fig. 10c | 347 |
| Copper Strip Array (d) Fig. 10d | 79 |
| Copper Strip Array (e) Fig. 10e | 331 |

pattern disappears almost completely. This could in principle be desirable for an application focusing solely on a region close to one edge of the imaging volume, such as the brain. The mode pattern farthest from the excitation is a result of the impedance discontinuity between the phantom and the air and would vanish in a longer or higher loss phantom.

In the second experiment with the $d = 15$ cm air gap, the copper strips and close distance results in a large amount of field coupled at the near end of the phantom compared with the rest. This shifts the scale and causes the image to appear almost blank as shown in Fig. 10(c). In an attempt to balance the field, the probe is pushed back to $d = 30$ cm, Fig. 10(d). This pattern is nearly identical to that of Fig. 10(d). With this structure and double the separation, the magnitude of the field coupled is much higher than in the case with no copper strip array, Fig. 10(a).

Creating a complete copper strip array that extends from the probe to the end of the phantom, yields an image with higher SNR and spreads the field more over the first 10 cm of the phantom, Fig. 10(e). The SNR is seven times higher than the case with no copper strip array, Fig 10(a), as shown in Table I. The large SNR improvement is a result of the copper strip array covering the air gap, while the mode change is due to the copper strip array covering the phantom. The SNR presented in Tables I and II is calculated using a 1-cm^2 square around the maximum field intensity.

It was found that the copper strip array has an impact when placed within 1 cm of the imaging volume. If it is placed any farther, the effect begins to diminish. Imaging a human with this setup poses a few difficulties. The strips must be placed in such a way that they do not irritate the patient, that is, they are placed away from sensitive areas, such as the ears, eyes, nose, and mouth. For a head scan, these can be placed primarily over the volume that encompasses the brain. Additionally, any metal in contact with the skin will cause a peak in specific absorption rate and undesired local heating. Simply placing a



Fig. 11. Setup for the multiple probe experiments showing an RHCP probe (right) and LHCP probe (left), placed 15 cm from the phantom edges.

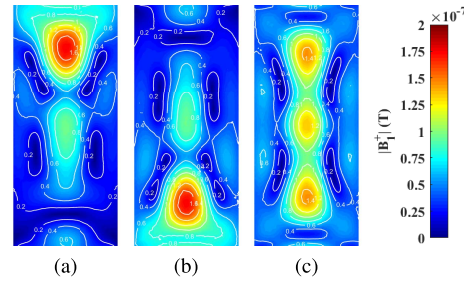


Fig. 12. Simulated results for relative phasing of (a) 180° , (b) 0° , and (c) 90° between the two probes, normalized to a total input power of 1 W.

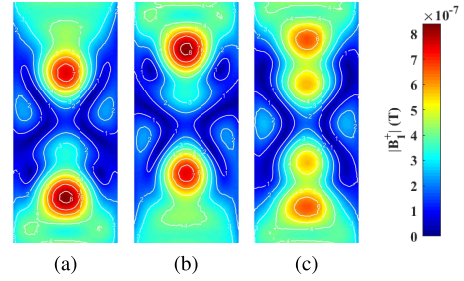


Fig. 13. Simulated results for relative phasing of (a) 180° , (b) 0° , and (c) 90° between the two probes with the added copper strip array, normalized to a total input power of 1 W. Note the field magnitude is four times higher than the case without a copper strip array in Fig. 12.

dielectric layer less than 0.5 cm thick under the strips reduces this peak inside the body without reducing the effect of the copper strip array.

IV. 7-T MULTIPLE PROBE TRANSMIT/RECEIVE RESULTS

An additional identical patch probe is placed on the opposite side of the phantom as seen in Fig. 11. This probe has the same dimensions as the original probe, but the feed is rotated 90° to accommodate the opposite polarization. This probe must be of opposite polarization to ensure that both probes excite the atomic spins in the same direction. Adding an extra probe to the system tests the use of B_1 shimming along with the effects of the copper strips.

By phasing the two probes 180° apart, Fig. 12(a) shows that the mode pattern can be shifted primarily to the top region. The field profile is now elongated and moved to the upper region of the phantom. The opposite is true when the probes are fed in phase. The mode pattern has now shifted toward the bottom of the phantom. When the probes are fed in quadrature,

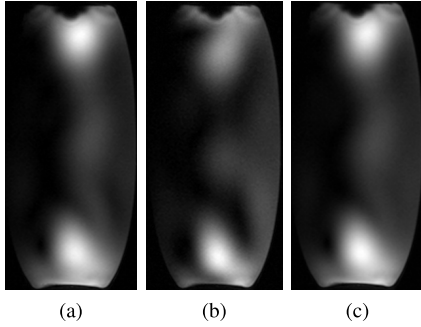


Fig. 14. Measured images for (a) receive only probe, (b) T/R probe, and (c) combined image of (a) and (b).

TABLE II
SNR FOR MULTIPLE PROBE EXPERIMENTS

| Experiment | SNR |
|---|-----|
| Receive Probe Fig. 14a | 235 |
| T/R Probe Fig. 14b | 226 |
| Combined Fig. 14c | 194 |
| B ₁ Shim Top Fig. 15a | 156 |
| B ₁ Shim Bottom Fig. 15b | 211 |
| B ₁ Shim Middle Fig. 15c | 192 |
| B ₁ Shim Copper Array Fig. 15d | 362 |

the modes merge in the center to create an extended center mode pattern. While the signal is now spread out over the majority of the phantom fairly evenly, bright spots still exist and need to be controlled. Constructive interference has created a higher peak field magnitude compared with the single probe case even with the same total input power.

Adding the copper strip array across both gaps and the phantom creates the mode structures shown in Fig. 13. The performance is similar to the single probe case with the copper strip array, Fig. 9(e). In this case, however, the peak signal is slightly lower and the field is more evenly distributed in the ends of the phantom.

The MR images from Fig. 14 show the case of one probe transmitting and both probes receiving. As expected, the lower mode pattern is brighter in every case due to the placement of the transmit probe. Similarly to the single probe case, the middle pattern tends toward the right (posterior) of the image. The mode pattern farthest from the excitation in Fig. 14(a) is much brighter than in the single probe case and in Fig. 14(b). This confirms reciprocity between the transmit and receive field patterns. Interestingly, the SNR is slightly lower in the combined case, as shown in Table II. This is most likely due to the additional noise present in combining the two images without any additional power. This SNR figure has increased dramatically compared with the single probe case; however, the setup, mainly the T/R switch module, and imaging parameters also changed between experiments.

The two transmitting probes allow B₁ shimming, which here consists in adjusting the relative phase of the excitations to create a region as homogeneous as possible. For this experiment, top, bottom, and center focusing regions were defined. From Fig. 15(c), B₁ shimming produces a more homogeneous signal in the center of the phantom connecting the two bright mode structures. The shift of the center mode is

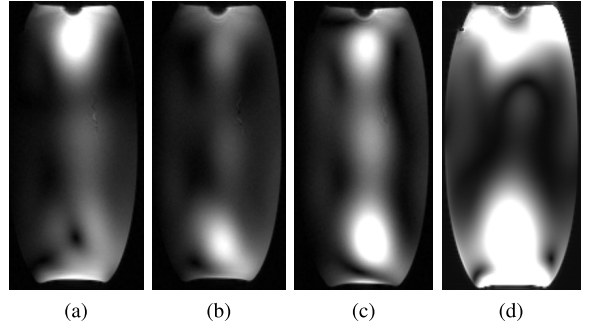


Fig. 15. B₁ shimming for regions. (a) Top region. (b) Bottom region. (c) Center region. (d) Added copper strip array.

also removed with this technique. The results show this probe can use the same B₁ shimming methods as classical structures.

Initially, the copper strip array is added to the system without attempting B₁ shimming. The image shown in Fig. 15(d) has structural similarity to the simulated field profile; Fig. 13(b) shows a noticeable SNR improvement over the two probe case and a broadening of the field similar to that seen in the single probe case with a copper strip array. The simulated field strength has a five times field strength increase over the initial case with one probe and no copper strip array. The actual result is 1.86 times higher than the SNR as the single transmit probe case, Fig. 14(c).

V. 10.5-T SIMULATED AND EXPERIMENTAL RESULTS

Traveling-wave excitation and detection systems in MRI can potentially be advantageous in terms of providing a more comfortable environment for patients, a larger field of view, imaging hard-to-reach organs (e.g., prostate gland) and some areas that are difficult to access with MRI, as well as enabling new spatial encoding schemes and a variety of mode sensitivity profiles [35]. As the wavelength decreases in size compared with the imaging volume, the quasi-static approach suffers. To illustrate this concept, a 7-T head coil tuned to work at 10.5 T (447 MHz) is imaged. A smaller phantom with a 12-cm diameter and 20-cm length is used as the imaging volume for the head coil. As shown in Fig. 16(a), inhomogeneity due to modes is present in the classical volume coil excitation. This mode structure is identical to the simulated patch probe excitation for the same phantom. This shows that, independent of the approach, similar mode patterns appear for a given phantom, indicating that similar solutions for improving field homogeneity could be applied to traveling-wave and classical excitations. However, the excited region for a traveling-wave excitation extends farther than in the case of near-field coil excitations [5].

A single patch probe is excited to observe the simplest case results at 10.5 T so they can be compared with simulations. The copper strip array is then wrapped around both the gap and the phantom. All images are taken using a gradient recalled echo sequence for an FOV of $16.25 \times 40 \text{ cm}^2$ with a small flip angle.

Experiments on the 10.5-T system use the same phantom and the probe seen in Fig. 1(c) (right). The probe is placed

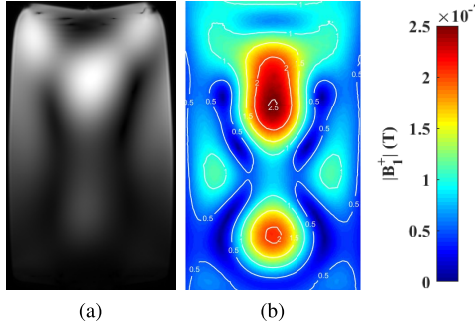


Fig. 16. (a) Tuned 7-T head volume coil MR image at 10.5 T. (b) Simulated patch probe excitation.

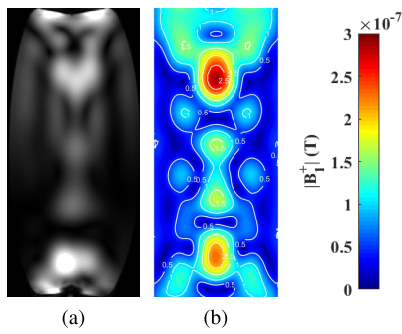


Fig. 17. Single probe experiment results for (a) MR image and (b) simulated patch probe excitation.

15 cm from the phantom, similar to setup of the 7-T experiments. Due to the increase in frequency, the mode pattern is more complicated compared with 7 T with the same phantom. However, the pattern obtained in the experimental MR image in Fig. 17(a) has strong similarity with the simulated image shown in Fig. 17(b). While some overall similarity can also be observed between field magnitude profiles observed at 7 and 10.5 T, the 10.5-T pattern clearly exhibits a more complex distribution that includes multiple local spots with high or very low field magnitude. The SNR of the experimental image was found to be 471.

It is found that a copper strip array does not improve field homogeneity since the electrical size of the bore and phantom is larger than at 7 T. It should be noted, however, that it is well known from experience that improving homogeneity in a uniform water-based dielectric phantom at high magnetic fields is typically very difficult, if not impossible. By contrast, the human head is a complex combination of different tissues, with an averaged relative permittivity $\epsilon_r \approx 55$ offering more flexibility in terms of B_1 field modulation. Using Sim4Life, the human body tissue numerical model of a male adult (Duke, IT'IS, Zurich, Switzerland) from the IT'IS virtual population is used to load the probe with and without a copper strip array (Fig. 18) at 447 MHz and to compute the resulting B_1 distribution. The copper strip array extends from the probe, follows the contour of the head, and stops at the ear. The copper strip array limits the field propagation to only the region of interest around the brain and expands the mode pattern to the areas with nulls. This will also constrain the E -field to this area.

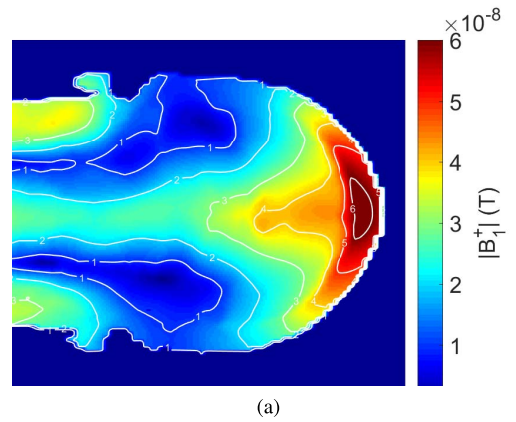


Fig. 18. Sim4Life simulated results using Duke from IT'IS virtual population (a) without copper strip array and (b) with copper strip array.

VI. NUMERICAL METHODOLOGY

Current simulation methods include complex physics modeling or a quasi-static approximation of the system [36]. The physics simulations model the excitations and response on an atomic level, thus requiring extensive computational resources and time. This approach is typically done with a finite-difference time-domain solver. For high field MRI, the frequency is too high to use the quasi-static approximation as the imaging volume is electrically large. For wide-bore MRI, the computational domain becomes much larger and must model the interactions between the RF excitation and the bore.

The goal of this analysis is to simplify the numerical problem without introducing significant additional error. Only one excitation and the transmit probe are modeled, since this adequately illustrates the problem, while introducing more excitations and boundary structures would further increase computational resources. This analysis is done using Ansys HFSS finite-element modeling with mixed order basis functions for the 10.5-T system. The time presented is total CPU time on a 3.6 GHz Intel i7-3820. To observe the effect of the bore, four different approaches are taken and results compared with a control case. The chosen control simulation is the complete system of the bore and gradient coil as shown in Fig. 1(b). An air box with a radiation boundary is placed around the bore. This simulation approximates the physical setup of the MRI and is shown in Fig. 17(b). To ensure

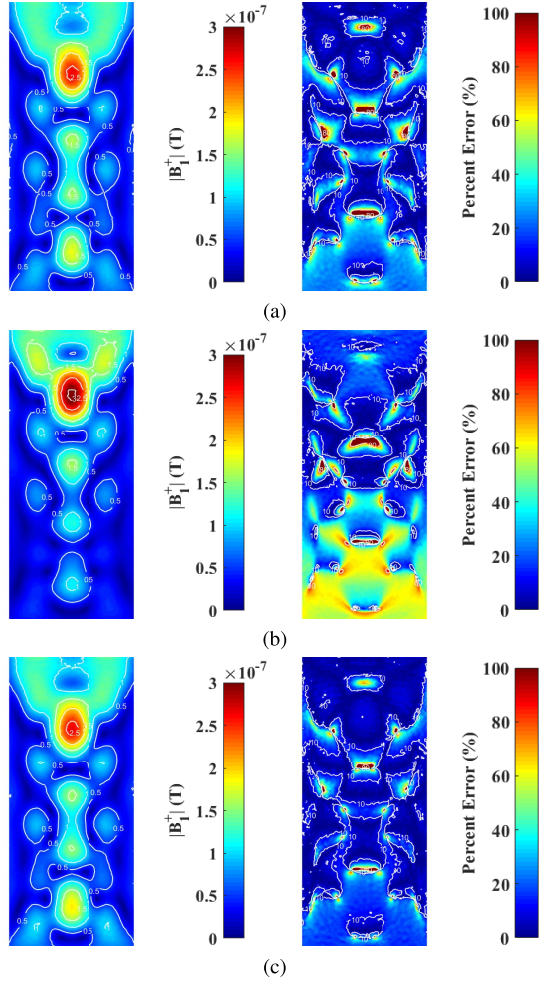


Fig. 19. Simulated results (left) and percent error (right) for (a) radiation boundary around the gradient coil, (b) no bore or gradient region present, and (c) radiation boundary on the end face of the gradient coil.

adequate mesh coverage and overlap for comparison, the maximum mesh size inside of the phantom is set at 1.5 cm. This simulation takes 1:37:05 (h:min:s) and requires 19.7 GB of RAM.

The first approach simply removes the bore from the simulation. The reasoning here is that the field from the probe diminishes relatively quickly, and thus, the bore has little effect. The resulting simulation can be seen on the left in Fig. 19(a) with the overall percent error shown on the right. The main difference from the control simulation lies in the gradient of the field intensity. The fields decay slightly slower resulting in a somewhat expanded mode pattern. This simulation is not much faster at 01:20:36 and uses 18 GB of RAM. With this approach, the average error across the field slice is 18.51%. This setup is important as not all software allow complete control over the outer boundary conditions.

The next approach removes the bore and gradient coil, leaving just the probe, phantom, and a radiation boundary. This reduces the simulation time down to 00:58:19 and a total RAM usage of 14.9 GB, but at great cost. As expected, the field profile significantly changes as shown in Fig. 19(b). The field propagation through the phantom is very poor and, overall,

TABLE III
SUMMARY OF RESULTS OF NUMERICAL STUDY

| Method | CPU Time (h:min:sec) | Memory (GB) | Percent Error (%) |
|---|----------------------|-------------|-------------------|
| Control Fig. 17b | 01:37:05 | 19.7 | N/A |
| Bore Removed Fig. 19a | 01:20:36 | 18 | 18.51 |
| No Bore/Gradient Coil Fig. 19b | 00:58:19 | 14.9 | 28 |
| Radiation Boundary on Bore Face | 01:14:05 | 16.8 | 12.33 |
| Radiation Boundary on Gradient Coil Face Fig. 19c | 00:57:33 | 14.1 | 12.42 |

does not match the experimental results shown in Fig. 17(a). This result clearly highlights the importance of the waveguide effects of the MRI system when using the excitation probes investigated in this paper. The average error is much higher at 28%.

The third approach keeps the bore and gradient coil in place, and adds a radiation boundary to the opening of the bore. This reduces the simulation time down to 01:14:05 with a total RAM usage of 16.8 GB. The reduction can be attributed to removing the overmodeled exterior of the system. The average error is lower at 12.33%. The plot is not shown, however, the results are nearly identical to the next approach in Fig. 19(c), where the bore is eliminated and radiation boundaries placed on the faces of the gradient region. This only slightly reduces the simulation time to 00:57:33 and RAM usage to 14.1 GB. The result shown in Fig. 19(c) matches the control simulation very well. The average error remains similar at 12.42%.

These simulations, summarized in Table III, are useful in providing an overall understanding of what to expect. While this simulation is relatively simple and short, the complexity must increase in order to improve the homogeneity of the excited B -field. This quickly increases the simulation time. Additional steps can be taken to improve the simulation by modifying HFSS solver parameters; however, these are specific to the application and will not be explored.

VII. CONCLUSION

This paper has shown single patch probe excitation benefits and difficulties. The patch probe can be placed a significant distance from the imaging volume ($d = 15\text{--}25$ cm) for improving patient comfort. Unfortunately with only a single probe, the spatial coverage for the received power is low and the image quality suffers. Using a copper strip array can improve the coupling for the transmit and receive, and depending on the structure, it can modify the excited modes inside the imaging volume. At 10.5 T, the copper strip array did not perform as well as expected compared with simulations. However, this is not surprising since it was designed for 7-T use. Further simulations will be necessary to determine how to optimize the approach at 447 MHz. Two patch probes were used to show benefits of B_1 shimming. By phasing two probes together with and without a copper strip array, the region of interest can be shifted along the phantom. These initial investigational setups described in this paper were not tailored to MRI clinical settings, and produced RF excitation that would not extend

through the whole human body. However, it is anticipated that further developments may result in better coverage, including phasing traveling-wave probes together as they wrap around the imaging volume.

REFERENCES

- [1] E. Haacke, R. Brown, M. Thompson, and R. Venkatesan, *Magnetic Resonance Imaging*. Hoboken, NJ, USA: Wiley, 2014, ch. 1, pp. 827–858.
- [2] P. B. Roemer, W. A. Edelstein, C. E. Hayes, S. P. Souza, and O. M. Mueller, “The NMR phased array,” *Magn. Reson. Med.*, vol. 16, no. 2, pp. 192–225, 1990.
- [3] J. T. Vaughan, H. P. Hetherington, J. O. Otu, J. W. Pan, and G. M. Pohost, “High frequency volume coils for clinical NMR imaging and spectroscopy,” *Magn. Reson. Med.*, vol. 32, no. 2, pp. 206–218, 1994.
- [4] R. H. Caverly, “MRI fundamentals: RF aspects of magnetic resonance imaging (MRI),” *IEEE Microw. Mag.*, vol. 16, no. 6, pp. 20–33, Jul. 2015.
- [5] D. Brunner, N. D. Zanche, J. Frohlich, J. Paska, and K. P. Pruessmann, “Travelling-wave nuclear magnetic resonance,” *Nature*, vol. 457, no. 7232, pp. 994–998, Feb. 2009.
- [6] A. G. Webb, C. M. Collins, M. J. Versluis, H. E. Kan, and N. B. Smith, “MRI and localized proton spectroscopy in human leg muscle at 7 Tesla using longitudinal traveling waves,” *Magn. Reson. Med.*, vol. 63, no. 2, pp. 297–302, 2010.
- [7] K. Haines *et al.*, “MR microimaging with a cylindrical ceramic dielectric resonator at 21.1T,” presented at the 51st ENC Experimental Nuclear Magn. Resonance Conf., Daytona Beach, FL, USA, Apr. 2010.
- [8] R. Fu *et al.*, “Ultra-wide bore 900 MHz high-resolution NMR at the national high magnetic field laboratory,” *J. Magn. Reson.*, vol. 177, no. 1, pp. 1–8, 2005.
- [9] V. Schepkin, W. W. Brey, and P. L. Gor, “kov, and S. C. Grant, “Initial *in vivo* rodent sodium and proton MR imaging at 21.1T,” *Magn. Reson. Imag.*, vol. 28, no. 3, pp. 400–407, 2010.
- [10] K. Uğurbil, “Magnetic resonance imaging at ultrahigh fields,” *IEEE Trans. Biomed. Eng.*, vol. 61, no. 5, pp. 1364–1379, May 2014.
- [11] F. H. Geschewski, D. Brenner, J. Felder, and N. J. Shah, “Optimum coupling and multimode excitation of traveling-waves in a whole-body 9.4T scanner,” *Magn. Reson. Med.*, vol. 69, no. 6, pp. 1805–1812, 2013.
- [12] A. Andreychenko, H. Kroese, D. W. Klomp, J. J. Lagendijk, P. R. Luijten, and C. A. van den Berg, “Coaxial waveguide for travelling wave MRI at ultrahigh fields,” *Magn. Reson. Med.*, vol. 70, no. 3, pp. 875–884, 2013.
- [13] A. Tonyushkin, J. A. Muniz, S. C. Grant, and A. J. M. Kiruluta, “Traveling wave mri in a vertical bore 21.1-T system,” in *Proc. Soc. Magn. Reson. Med.*, Melbourne, VIC, Australia, May 2012, p. 2693.
- [14] A. A. Tonyushkin, N. B. Konyer, M. D. Noseworthy, and A. J. M. Kiruluta, “Imaging with dielectric waveguide approach for 3T MRI,” *Int. Soc. Magn. Reson. Med.*, Melbourne, VIC, Australia, May 2012, p. 2698.
- [15] J. A. Tang, G. C. Wiggins, D. K. Sodickson, and A. Jerschow, “Cutoff-free traveling wave NMR,” *Concepts Magn. Reson. A*, vol. 38A, no. 5, pp. 253–267, 2011.
- [16] W. Koning *et al.*, “High-resolution MRI of the carotid arteries using a leaky waveguide transmitter and a high-density receive array at 7 T,” *Magn. Reson. Med.*, vol. 69, no. 4, pp. 1186–1193, 2013.
- [17] Ö. Ipek, A. J. E. Raaijmakers, D. W. J. Klomp, J. J. W. Lagendijk, P. R. Luijten, and C. A. T. van den Berg, “Characterization of transceive surface element designs for 7 Tesla magnetic resonance imaging of the prostate: Radiative antenna and microstrip,” *Phys. Med. Biol.*, vol. 57, no. 2, p. 343, 2012.
- [18] A. Andreychenko, H. Kroese, V. O. Boer, J. J. W. Lagendijk, P. R. Luijten, and C. A. T. van den Berg, “Improved steering of the RF field of traveling wave MR with a multimode, coaxial waveguide,” *Magn. Reson. Med.*, vol. 71, no. 4, pp. 1641–1649, 2014.
- [19] J. Hoffmann, G. Shajan, J. Budde, K. Scheffler, and R. Pohmann, “Human brain imaging at 9.4 T using a tunable patch antenna for transmission,” *Magn. Reson. Med.*, vol. 69, no. 5, pp. 1494–1500, 2013.
- [20] M. Kozlov and R. Turner, “Analysis of RF transmit performance for a 7T dual row multichannel MRI loop array,” in *Proc. Annu. Int. Conf. IEEE Eng. Med. Biol. Soc.*, Aug. 2011, pp. 547–553.
- [21] A. J. E. Raaijmakers *et al.*, “Design of a radiative surface coil array element at 7 T: The single-side adapted dipole antenna,” *Magn. Reson. Med.*, vol. 66, no. 5, pp. 1488–1497, 2011.
- [22] G. Shajan, J. Hoffmann, D. Z. Balla, D. K. Deelchand, K. Scheffler, and R. Pohmann, “Rat brain MRI at 16.4T using a capacitively tunable patch antenna in combination with a receive array,” *NMR Biomed.*, vol. 25, no. 10, pp. 1170–1176, 2012.
- [23] S.-M. Sohn, L. DelaBarre, A. Gopinath, and J. T. Vaughan, “RF head coil design with improved RF magnetic near-fields uniformity for magnetic resonance imaging (MRI) systems,” *IEEE Trans. Microw. Theory Techn.*, vol. 62, no. 8, pp. 1784–1789, Aug. 2014.
- [24] B. Wu *et al.*, “Multi-channel microstrip transceiver arrays using harmonics for high field MR imaging in humans,” *IEEE Trans. Med. Imag.*, vol. 31, no. 2, pp. 183–191, Feb. 2012.
- [25] A. J. Raaijmakers *et al.*, “The fractionated dipole antenna: A new antenna for body imaging at 7 Tesla,” *Magn. Reson. Med.*, vol. 75, no. 3, pp. 1366–1374, 2016.
- [26] M. Ilic, A. Tonyushkin, N. Sekeljic, P. Athalye, and B. M. Notaros, “RF excitation in 7 Tesla MRI systems using monofilar axial-mode helical antenna,” in *Proc. Int. Symp. Antennas Propag. USNC/URSI Nat. Radio Sci. Meeting*, Jul. 2015, pp. 1346–1347.
- [27] G. Adriany *et al.*, “Transmit and receive transmission line arrays for 7 Tesla parallel imaging,” *Magn. Reson. Med.*, vol. 53, no. 2, pp. 434–445, 2005.
- [28] P. Bluem *et al.*, “Travelling-wave excitation for 16.4T small-bore MRI,” in *IEEE MTT-S Int. Microw. Symp. Dig.*, May 2015, pp. 1–4.
- [29] S. Ramo, J. R. Whinnery, and T. V. Duizer, *Fields and Waves in Communication Electronics*. Hoboken, NJ, USA: Wiley, 1994.
- [30] I. A. Elabyad, A. Omar, T. Herrmann, J. Mallon, and J. Bernardino, “Travelling wave approach for high field magnetic resonance imaging,” in *Proc. IEEE 3rd Int. Symp. Appl. Sci. Biomed. Commun. Technol. (ISABEL)*, Nov. 2010, pp. 1–5.
- [31] X. L. Bao and M. J. Ammann, “Compact annular-ring embedded circular patch antenna with cross-slot ground plane for circular polarisation,” *Electron. Lett.*, vol. 42, no. 4, pp. 192–193, Feb. 2006.
- [32] E. Lier and P.-S. Kildal, “Soft and hard horn antennas,” *IEEE Trans. Antennas Propag.*, vol. 36, no. 8, pp. 1152–1157, Aug. 1988.
- [33] G. Ruvio, P. S. Kildal, and S. Maci, “Modal propagation in ideal soft and hard waveguides,” in *Proc. IEEE Antennas Propag. Soc. Int. Symp.*, vol. 4, Jun. 2003, pp. 438–441.
- [34] O. Dietrich, J. G. Raya, S. B. Reeder, M. F. Reiser, and S. O. Schoenberg, “Measurement of signal-to-noise ratios in MR images: Influence of multichannel coils, parallel imaging, and reconstruction filters,” *J. Magn. Reson. Imag.*, vol. 26, no. 2, pp. 375–385, 2007.
- [35] A. J. M. Kiruluta, “The emergence of the propagation wave vector in high field NMR: Analysis and implications,” *J. Phys. D, Appl. Phys.*, vol. 40, no. 10, p. 3043, 2007.
- [36] R. K. S. Kwan, A. C. Evans, and G. B. Pike, “MRI simulation-based evaluation of image-processing and classification methods,” *IEEE Trans. Med. Imag.*, vol. 18, no. 11, pp. 1085–1097, Nov. 1999.

Patrick Bluem (S’14–GS’14) received the B.S. and M.S. degrees in electrical engineering from the University of Colorado Boulder, Boulder, CO, USA, in 2014 and 2016, respectively, where he is currently pursuing the Ph.D. degree under Z. Popović.

Andrew Kiruluta, photograph and biography not available at the time of publication.



Pierre-Francois Van de Moortele received the M.D. and Ph.D. degrees.

He has been involved for about two decades in magnetic resonance imaging methods in humans with a focus on scanners operating at high (three Tesla) and ultrahigh (seven Tesla) magnetic fields. He then joined the Center for Magnetic Resonance Research (CMRR), University of Minnesota, Minneapolis, MN, USA, where he pursued his research at 7T and 9.4T, developing multiple approaches to address transmit B1 heterogeneity

in multichannel head and body transmit RF arrays for a large range of human applications with a special emphasis on cardiovascular and cerebral targets. He is currently an Associate Professor with the Center for Magnetic Resonance Research (CMRR), University of Minnesota. He is also investigating transmit B1 issues on a 10.5 T system, which is currently the largest available whole body human MR scanner. He has co-authored over 100 peer-reviewed articles related with MRI. His research began in Paris, France, developing acquisition methods for fast imaging on a 3-T system.



Gregor Adriany (M'14) received the M.S. and Ph.D. (Dr.Ing) degrees in electrical engineering from the University RWTH Aachen, Aachen, Germany, in 1993 and 1998, respectively.

He is currently an Associate Professor with the Department of Radiology, Center for Magnetic Resonance Research, University of Minnesota, Minneapolis, MN, USA. He has a broad background in high-frequency design particularly related to MRI coils and antennas. His pioneering work related to UHF transmit arrays has resulted in numerous highly

cited publications and patents. His current research interests include optimized antenna and technology development for ultrahigh frequency human MRI applications.



Zoya Popović (S'86–M'90–SM'99–F'02) received the Dipl.Ing. degree from the University of Belgrade, Serbia, in 1985, and the Ph.D. degree from the California Institute of Technology, Pasadena, CA, USA, in 1990.

She was named the 2015 Distinguished Research Lecturer with the University of Colorado Boulder, Boulder, CO, USA. In 2001/03 and 2014, she was a Visiting Professor with the Technical University of Munich, Munich, Germany, and with the Institut supérieur de l'aéronautique et de l'espace,

Toulouse, France, respectively. Since 1991, she has graduated 56 Ph.D. students and currently leads a group of 16 doctoral students and two Post-Doctoral Fellows. Since 1990, she has been with the University of Colorado Boulder, where she is currently a Distinguished Professor and holds the Hudson Moore Jr. Endowed Chair with the Department of Electrical, Computer and Energy Engineering. Her current research interests include high-efficiency transmitters for radar and communication, low-noise and broadband microwave and millimeter-wave circuits, antenna arrays, wireless powering for batteryless sensors and medical applications of microwaves such as core-body thermometry and traveling-wave MRI.

Dr. Popović was elected a Foreign Member of the Serbian Academy of Sciences and Arts in 2006. She was a recipient of the 1993 and 2006 IEEE MTT-S Microwave Prizes for the best journal papers, the 2000 Humboldt Research Award for Senior U.S. Scientists from the German Alexander von Humboldt Stiftung, the 2001 Hewlett-Packard/American Society for Engineering Education Terman Medal for combined teaching and research excellence. In 2013, she was named the IEEE MTT-S Distinguished Educator. She was also the recipient of the 1996 URSI Isaac Koga Gold Medal and was named an NSF White House Presidential Faculty Fellow in 1993.

Allison Duhamel (S'13–M'14) received the B.Sc. degree in electrical engineering from Columbia University, New York, NY, USA, in 2014. She is currently pursuing the Ph.D. degree at the University of Colorado Boulder, Boulder, CO, USA.

From 2014 to 2015, she was a Fellow of the 31st Congress-Bundestag Youth Exchange Program, and completed a visiting semester with the Technical University of Munich, Munich, Germany, and a research internship with Perisens GmbH, Munich.